

Metal–Insulator Transitions in $\text{La}_{1-x}\text{TiO}_3$, $0.0 \leq x \leq 0.33$. Structure–Property Correlations

M. J. MacEachern, H. Dabkowska, J. D. Garrett, G. Amow, Wenhe Gong,
Guo Liu, and J. E. Greedan*

Department of Chemistry and Institute for Materials Research, McMaster University,
Hamilton, Canada L8S 4M1

Received May 16, 1994. Revised Manuscript Received August 10, 1994[®]

The solid-solution system $\text{La}_{1-x}\text{TiO}_3$ was investigated over the range $0 \leq x \leq 0.33$, i.e., involving end members LaTiO_3 and $\text{La}_{2/3}\text{TiO}_3$. X-ray single-crystal and powder neutron diffraction studies have established the structure of $\text{La}_{2/3}\text{TiO}_3$ for the first time which is described in *Pban* with $a = 5.461(1)$ Å, $b = 5.482(1)$ Å, $c = 7.759(3)$ Å. La vacancies are ordered largely in the $z = 1/2$ plane and Ti atoms are displaced from the centers of Ti–O octahedra toward this plane giving rise to *c*-axis chains consisting of two short Ti–O bonds (1.906 Å) alternating with two long Ti–O bonds (1.975 Å). The *Pban* structure is found for $0.25 < x \leq 0.33$, an *Ibmm* structure for $0.20 < x \leq 0.25$ and the *Pbnm* (GdFeO_3 type) structure for $0 \leq x < 0.20$. The compounds $\text{La}_{2/3}\text{TiO}_3$ ($x = 0.33$) and $\text{La}_{0.70}\text{TiO}_3$ ($x = 0.30$) are insulators, $\text{La}_{0.75}\text{TiO}_3$ ($x = 0.25$) undergoes a metal–insulator transition and $\text{La}_{0.80}\text{TiO}_3$ ($x = 0.20$) to $\text{La}_{0.92}\text{TiO}_3$ ($x = 0.08$) are metallic. Electrical, magnetic and structural properties are compared with those of the closely related $\text{La}_{1-x}\text{Sr}_x\text{TiO}_3$ and SrTiO_{3-x} systems. It is also argued that oxidized forms of LaTiO_3 , described previously as LaTiO_{3+x} , are better understood as $\text{La}_{1-x}\text{TiO}_3$.

Introduction

There has been renewed interest, recently, in perovskite type transition metal oxides with small d-electron/ion ratios, e.g., d^1 and d^2 as analogues of the cuprate superconductors. Of particular interest here are the several studies based on the d^1 system LaTiO_3 and the d^0 systems SrTiO_3 and BaTiO_3 in which the electron count is varied by the formation of solid solutions $\text{La}_{1-x}\text{M}_x\text{TiO}_3$, $\text{M} = \text{Sr}, \text{Ba}$,^{1–6} by reducing SrTiO_3 ,⁷ or by oxidizing LaTiO_3 , e.g., LaTiO_{3+x} ,^{8,9} and $\text{La}_{1-x}\text{TiO}_3$.^{10,11}

LaTiO_3 itself was first reported in 1954,¹² but it was not until 1979 that its structure was determined to be of the GdFeO_3 type, *Pbnm* (*Prma*), from X-ray diffraction studies on a melt-grown, highly twinned crystal.¹³

This structure was verified and the refinement improved at room temperature from Rietveld analysis of high-resolution neutron powder diffraction data and, as well, the low-temperature evolution of the structure was studied with no apparent change in symmetry seen to 10 K.¹⁴

LaTiO_3 was characterized as a material near a metal to semiconductor transition and a long-range ordered AF state was found below 125 K in the twinned crystalline samples studied.¹⁵

More recent work has established that reasonably stoichiometric LaTiO_3 is semiconducting or insulating and that the AF transition can occur at temperatures as high as 140–150 K.^{8,9} Stoichiometric LaTiO_3 is best regarded as a Mott Hubbard insulator.

It was reported recently that LaTiO_3 can be oxidized, LaTiO_{3+x} , with a maximum $x \approx 0.20$ and still retain the orthorhombic perovskite structure.⁸ It is difficult to understand how this description of the nonstoichiometry can be taken literally as the perovskite structure consists of close packed layers of LaO_3 with Ti ions ordered in one-quarter of the octahedral sites. There is no obvious site for a large interstitial anion, O^{2-} . It is much more likely that oxidation occurs via the formation of La^{3+} vacancies formulated as $\text{La}_{1-x}\text{TiO}_3$. Evidence for this has been presented for single crystals grown from the melt under conditions similar to those used in ref 8 and additional evidence will be advanced later in this work.¹¹ Furthermore the grossly La-deficient compound $\text{La}_{2/3}\text{TiO}_3$ in which titanium is fully oxidized to the +4 state, $3d^0$, has been known since 1955, and compositions of the solid solution $\text{La}_{1-x}\text{TiO}_3$ have been prepared and studied.¹⁶ The complete solid

[®] Abstract published in *Advance ACS Abstracts*, October 1, 1994.

- (1) Sunstrom IV, J. E.; Kauzlarich, S. M.; Klavins, P. *Chem. Mater.* **1992**, *4*, 346.
- (2) Sunstrom IV, J. E.; Kauzlarich, S. M. *Chem. Mater.* **1993**, *5*, 1539.
- (3) Higuchi, M.; Aizawa, K.; Yamaya, K.; Kodaira, K. *J. Solid State Chem.* **1991**, *92*, 573.
- (4) Tokura, Y.; Taguchi, Y.; Okada, Y.; Fujishima, Y.; Arima, J.; Iye, Y.; Kumagai, K. *Phys. Rev. Lett.* **1993**, *70*, 2126.
- (5) Kumagai, K.; Suzuki, T.; Taguchi, Y.; Okada, Y.; Fujishima, Y.; Tokura, Y. *Phys. Rev.* **1993**, *B48*, 7636.
- (6) Eylem, C.; Saghi-Szabo, G.; Chen, B.-H.; Eichorn, B.; Peng, J.-L.; Greene, R.; Salamanca-Riba, L.; Nahm, S. *Chem. Mater.* **1992**, *4*, 1038.
- (7) Gong, W.; Yun, H.; Ning, Y. B.; Greedan, J. E.; Datars, W. R.; Stager, C. V. *J. Solid State Chem.* **1991**, *90*, 320.
- (8) Lichtenberg, F.; Widmer, D.; Bednorz, J. G.; Williams, T.; Reller, A. *Z. Phys. B, Cond. Matter* **1991**, *B2*, 211.
- (9) Okada, Y.; Arima, T.; Tokura, Y.; Murayama, C.; Môri, N. *Phys. Rev.* **1993**, *B48*, 9677.
- (10) Crandles, D. A.; Timusk, T.; Greedan, J. E. *Phys. Rev.* **1991**, *B44*, 13250.
- (11) Crandles, D. A.; Timusk, T.; Garrett, J. D.; Greedan, J. E. *Phys. Rev. B* **1994**, *49*, 16207.
- (12) Kestigian, M.; Ward, R. *J. Am. Chem. Soc.* **1954**, *76*, 6027.
- (13) MacLean, D. A.; Ng, H.-N.; Greedan, J. E. *J. Solid State Chem.* **1979**, *30*, 35.

(14) Eitel, M.; Greedan, J. E. *J. Less Common Met.* **1986**, *116*, 95.

(15) MacLean, D. A.; Greedan, J. E. *Inorg. Chem.* **1981**, *20*, 1025.

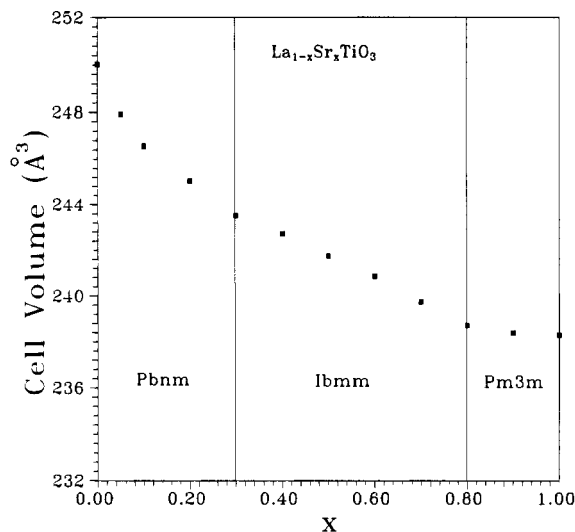


Figure 1. Dependence of the cell volume on x in $\text{La}_{1-x}\text{Sr}_x\text{TiO}_3$, crystallographic phase boundaries are indicated. Data compiled from ref 1. Volumes in the $Pm3m$ region have been multiplied by four to allow comparison with the $Pbnm$ and $Ibmm$ values.

solution between the two end members, $\text{La}_{1-x}\text{TiO}_3$ where $0 \leq x \leq 0.33$ has not been studied systematically, however. The results of electrical transport, magnetic, and optical reflectivity studies on single crystals within the composition range $0 \leq x \leq 0.12$ have been published elsewhere, and it is the aim of the present work in part to present structural characterization of these materials.¹¹

The detailed crystal structure of $\text{La}_{2/3}\text{TiO}_3$ has, surprisingly, not been reported, although orthorhombic symmetry has been proposed from an early X-ray powder diffraction study with unit cell constants $a = 3.869 \text{ \AA}$, $b = 3.882 \text{ \AA}$, $c = 7.796 \text{ \AA}$.¹⁷ But, flux-grown single crystals have more recently been described as cubic or tetragonal,¹⁸ so much confusion exists currently regarding the true structure of $\text{La}_{2/3}\text{TiO}_3$, and this issue will be addressed in this study.

The system $\text{La}_{1-x}\text{TiO}_3$ is thus analogous electronically and perhaps structurally to the aforementioned solid solutions, $\text{La}_{1-x}\text{Sr}_x\text{TiO}_3$ and $\text{La}_{1-x}\text{Ba}_x\text{TiO}_3$. The most widely studied and best characterized system is the former, $\text{La}_{1-x}\text{Sr}_x\text{TiO}_3$. The results of the most detailed structural study,¹ are shown in Figure 1. Compositions near both end members have the characteristic $Pbnm$ (LaTiO_3) or $Pm3m$ (SrTiO_3) structure but for intermediate compositions a $Ibmm$ cell is found. Note that the cell volume is not a linear function of x , and there are apparent changes in slope at the crystallographic phase boundaries.

A summary of the consensus electrical transport properties, displayed as a function of the Ti^{3+} concentration, is shown in Figure 2. The semiconducting or insulating behavior for LaTiO_3 , $x = 0.0$, 100% Ti^{3+} gives way to metallic properties for $x \approx 0.05$, 95% Ti^{3+} . Metallic character persists at least to the composition $x = 0.95$, 5% Ti^{3+} , for single-crystal samples, and it is

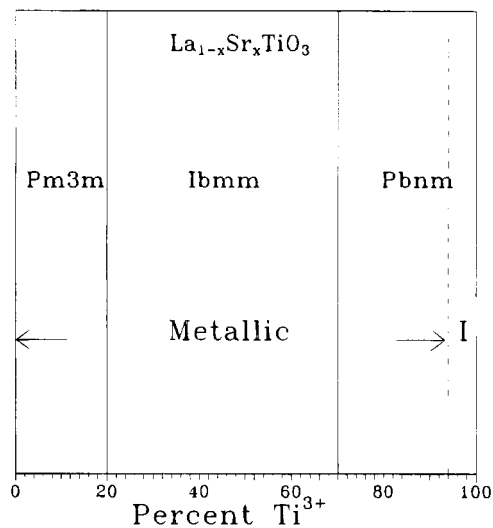


Figure 2. Comparison of the crystal structure and electrical properties as a function of Ti^{3+} concentration for $\text{La}_{1-x}\text{Sr}_x\text{TiO}_3$. Data compiled from refs 1, 3, 4, and 5.

likely to obtain for even larger x values. SrTiO_3 , $x = 1.0$ is of course insulating but very small doping levels of $9 \times 10^{19} \text{ electrons cm}^{-3}$, which would correspond to $x \approx 0.98$, 2% Ti^{3+} , in this series, are known to induce metallic and even superconducting properties.¹⁹ There exists one dissenting report which states that the $x = 0.9$, 10% Ti^{3+} , phase is semiconducting.¹ Further detailed comparisons with the $\text{La}_{1-x}\text{Sr}_x\text{TiO}_3$ series will be made later.

A similar comparison with published results for the LaTiO_{3+x} system⁸ is rendered difficult due to reasons which will be outlined later. Qualitatively, the electrical transport behavior mirrors that of the previously discussed system with semiconducting or insulating behavior for small Ti^{4+} levels giving way to metallic behavior.

There exists considerably less consensus regarding the structural and physical properties of the related $\text{La}_{1-x}\text{Ba}_x\text{TiO}_3$ series. In one case complete solid solubility is reported up to $x = 0.5$ with the same $Pbnm-Ibmm$ phase sequence as for the Sr series,² while in another study of the same composition range, an extensive two-phase region is seen.⁶ There is also significant diversity in electrical transport behavior with some samples showing unusual effects which are attributed to particle size.²

One final system relevant to the $\text{La}_{1-x}\text{TiO}_3$ series is the recently described, grossly nonstoichiometric, SrTiO_{3-x} with $x = 0.08$, 0.17, and 0.28.⁷ These materials remain cubic, $Pm3m$, in spite of high Ti^{3+} and O^{2-} vacancy levels, although quenched $x = 0.28$ samples show a metastable tetragonal distortion. All are metallic but evidence of carrier localization is seen in the form of a large discrepancy between the expected carrier density based on the measured oxygen defect level and that measured from the Hall effect.

In this study it is established that a solid solution $\text{La}_{1-x}\text{TiO}_3$ exists for the full range, $0.0 \leq x \leq 0.33$, crystal structures are determined, and electrical and magnetic properties are measured, correlated with the structures, and compared with those of the related

(16) Kestigian, M.; Ward, R. J. *Am. Chem. Soc.* **1955**, *77*, 6199. Bazuev, G. V.; Makarova, O. V.; Shveikin, G. P. *Inorg. Mater.* **1983**, *19*, 92.

(17) Abe, M.; Uchino, K. *Mater. Res. Bull.* **1974**, *9*, 147.

(18) Yokoyama, M.; Ota, T.; Yamai, I.; Takahashi, J. *J. Cryst. Growth* **1989**, *96*, 490.

(19) Koonce, C. S.; Cohen, M. L.; Schooley, J. F.; Hosler, W. R.; Pfeiffer, E. R. *Phys. Rev.* **1967**, *163*, 380.

systems just described and with the single-crystal results mentioned previously.

Experimental Section

Preparation of Materials. Powders. La_{0.67}TiO₃: Starting materials were TiO₂ (99.9%) and La₂O₃ (99.9%) which had been pre-fired at 900 °C for 24 h to decompose any hydroxide or carbonate contaminants. A 1:3 molar mixture of La₂O₃ and TiO₂ was ground well under acetone in an agate mortar and pestle and pressed into 1/2 in. diameter pellets of ~2–3 g each. The pellets were fired in air at 1430 °C in alumina boats for 1 h, and upon cooling it was found that they consisted of an outer yellow portion and an inner gray portion. The pellets were reground, repressed, and fired at 1400 and then at 1390 °C again for 1 h, including an intermediate regrinding. The product obtained at 1390 °C was yellow throughout. An X-ray powder diffraction analysis indicated the presence of a small amount of a second phase.

La_{0.70}TiO₃–La_{0.92}TiO₃: The starting materials were La₂O₃, TiO₂, and Ti₂O₃. The latter was prepared by arc melting TiO₂ and Ti metal in an argon atmosphere. TGA results on the product showed that the true composition was Ti₂O_{3,024}. Well-ground and well-mixed powders of the starting materials were prepared by weighing appropriate amounts for target La/Ti ratios of 0.70, 0.75, 0.80, 0.88, and 0.92. In calculating the weights, account was taken of the measured composition of the Ti₂O₃ and a small additional amount of the more reduced oxide was added to compensate for oxidation during the firing process as determined by experience. Following mixing and grinding, the powders were pressed into pellets, loaded into an open Mo crucible, and covered with a ZrN disk. The crucible was mounted inside an induction coil in an rf heating apparatus and evacuated to a level of 3×10^{-4} Torr.

The samples were then heated by induction in a vacuum of $(2-3) \times 10^{-4}$ Torr for 12–18 h at 1250 °C for La_{0.70} and 1450 °C for the other samples. One regrinding and refiring under the same conditions was sufficient to produce materials which were single-phase via X-ray powder diffraction analysis. The color of the La_{0.70} phase was gray, and the others were black.

Single Crystals. La_{0.67}TiO₃: These crystals were grown from a KF–Na₂B₄O₇ flux according to published procedures.¹⁸ The following amounts in grams of starting materials were loaded into a 20 cm³ platinum crucible: TiO₂, 2.40; La₂O₃, 1.69; KF, 13.4; Na₂B₄O₇, 4.0; La₂O₃, 1.69; KF, 13.4; Na₂B₄O₇, 4.0. The covered mixture was heated at 1000 °C for 48 h. During this period a weight loss of about 20% was observed indicating flux evaporation. Transparent, yellow crystals of roughly rectangular cross section, typical size $0.5 \times 0.5 \times 1$ mm³, were found after hot pouring of the flux. The crystals adhered rather strongly to the crucible walls making recovery difficult.

La_{0.75}TiO₃ and La_{0.80}TiO₃: Crystals were grown from the melt by the Czochralski method in a modified Tri Arc electric arc furnace. Starting materials were polycrystalline pellets of the same nominal compositions.

Thermal Gravimetric Analysis. Thermal gravimetric analysis was carried out in a Netzsch STA 409 thermal balance under an atmosphere of flowing air at 1000 °C. The resulting samples were off-white in color. The results are reported in the following format, x in La_{1-x}TiO₃, observed percent weight gain (calculated percent weight gain), composition assuming nominal x : 0.08, 2.79 (2.72) La_{0.92}TiO_{2.99}; 0.12, 2.58 (2.35), La_{0.88}TiO_{2.97}; 0.20, 1.57 (1.55), La_{0.80}TiO_{2.99}; 0.25, 1.03 (1.00) La_{0.75}TiO_{2.99}; 0.30, 0.37 (0.41) La_{0.70}TiO_{3,005}. All compositions are slightly reduced in oxygen content except for $x = 0.30$ which is slightly oxidized. In no case does the oxygen content differ from the ideal value of 3.00 per formula unit by more than 1%. The error in the experimental percent weight gain is estimated to be ± 0.05 .

X-ray Powder Diffraction. All powder samples were analyzed initially, using an IRDAB Model XDC700 Guinier-Haag camera with Cu K α_1 radiation and a silicon internal standard. The films were measured with a KEJ Instruments model LS20 laser line scanner interfaced with a PC which produces directly a digitized data file. The data were reduced

Table 1. Cell Parameters Calculated from Guinier Powder Diffraction Data for La_{1-x}TiO₃

comp	space group	a (Å)	b (Å)	c (Å)	vol (Å ³)
La _{0.67} TiO ₃	<i>Pban</i>	5.482(1)	7.759(3)	5.461(1)	232.28(9)
La _{0.67} TiO ₃	<i>Pban</i>	5.477(1)	7.763(1)	5.461(2)	232.19(8) ^a
La _{0.70} TiO ₃	<i>Pban</i>	5.464(2)	7.777(2)	5.512(1)	234.22(10)
La _{0.75} TiO ₃	<i>Imma</i>	5.527(1)	7.793(2)	5.516(1)	237.58(8)
La _{0.75} TiO ₃	<i>Imma</i>	5.541(1)	7.793(1)	5.528(1)	238.70(6) ^a
La _{0.80} TiO ₃	<i>Imma</i>	5.557(1)	7.817(1)	5.532(1)	240.30(6)
La _{0.80} TiO ₃	<i>Imma</i>	5.556(1)	7.826(4)	5.518(2)	239.93(13) ^a
La _{0.88} TiO ₃	<i>Pnma</i>	5.582(1)	7.882(3)	5.559(1)	244.58(9)
La _{0.92} TiO ₃	<i>Pnma</i>	5.606(1)	7.914(1)	5.584(1)	247.74(7)
La _{1.0} TiO ₃	<i>Pnma</i>	5.607(1)	7.9175(1)	5.6247(1)	249.70 ^b

^a Data obtained from ground single crystal. ^b Reference 14.

with the program SCANPI, and cell refinement and indexing were effected with the program LSUDF.

Data suitable for profile refinement were collected on a Nicolet (Siemens) I2 diffractometer with Cu K α radiation.

Neutron Powder Diffraction. Powder neutron diffraction studies were carried out at the McMaster University Nuclear Reactor.

Radiation obtained from the (200) reflection of a copper single-crystal monochromator, giving a neutron wavelength of 1.3925 Å, was used for the data collection. The diffracted neutron beams were detected with a position-sensitive detector (PSD) which has been described previously.²⁰

A thin-walled vanadium can was used to contain the sample during the diffraction experiment. The can was 8 mm in diameter and filled with approximately 8 g of sample to a total volume of 1.5 cm³. All of the data were collected at room temperature under a vacuum of $\approx 10^{-3}$ Torr.

Data were refined using a version of the Rietveld Profile Refinement program DBWS 9600PC.

Magnetic Susceptibility. Magnetic susceptibility measurements were carried out on a Quantum Design superconducting quantum interference device (SQUID) magnetometer. All of the samples were sintered pellets with a typical sample size of 200 mg. Susceptibility measurements were taken in the temperature range 5–300 K with an applied magnetic field strength of 2000 Oe.

Electrical Resistivity. Electrical resistivity measurements were taken on a number of samples. All of the samples except La_{0.80}TiO₃ were sintered rectangular pellets with a typical sample thickness of 0.8 cm. The La_{0.80}TiO₃ sample was a cylindrical single crystal with a thickness of 0.85 cm.

All the measurements were taken by a four-probe Van der Pauw method in the temperature range of 300–5 K by lowering the sample into a dewar of liquid helium.

Single-Crystal X-ray Diffraction. Crystals suitable for structure analysis were mounted on tips of glass fibers using epoxy cement. Data were collected on a Siemens P3 four-circle diffractometer with Ag K α radiation. Data reduction and structure solution were also performed on an 80486 PC using the Siemens SHELXTL PC software package. Scattering factors of neutral atoms have been employed. Crystal structures were refined using the program SHELXL, part of the SHELXL-92 γ -test version released in 1993. SHELXL refines crystal structures against F^2 instead of the conventional F data. As a result the $wR2$ factor is usually significantly higher than the conventional R ($R1$ in SHELXL).

Results and Discussion

Crystal Structures: La_{1-x}TiO₃. All samples except polycrystalline La_{2/3}TiO₃ were prepared in single phase form. Unit-cell constants were refined for all of the compositions studied from the Guinier-Haag data and are listed in Table 1. In all cases metrically orthorhombic cells were found with dimensions $a \approx \sqrt{2}a_c$,

Table 2. Atomic and Thermal Parameters Refined from Powder Neutron Diffraction Data for $\text{La}_{0.88}\text{TiO}_3$ and $\text{La}_{0.92}\text{TiO}_3$ in $Pnma^a$

		$\text{La}_{0.92}\text{TiO}_3$	$\text{La}_{0.88}\text{TiO}_3$
La	<i>x</i>	0.0384(6)	0.0288(9)
	<i>y</i>	$1/4$	$1/4$
	<i>z</i>	0.9891(11)	0.9970(18)
	<i>B</i> (\AA^2)	0.4	0.84(7)
Ti	occ	0.92	0.88
	<i>x</i>	$1/2$	$1/2$
	<i>y</i>	0	0
	<i>z</i>	0	0
O1	<i>B</i> (\AA^2)	0.40(1)	0.12(9)
	<i>x</i>	0.4885(11)	0.4937(15)
	<i>y</i>	$1/4$	$1/4$
	<i>z</i>	0.0829(15)	0.0476(17)
2	<i>B</i> (\AA^2)	1.1(1)	0.72(11)
	<i>x</i>	0.2848(8)	0.2776(15)
	<i>y</i>	0.0379(6)	0.0400(8)
	<i>z</i>	0.7116(8)	0.7154(13)
	<i>B</i> (\AA^2)	0.57(7)	1.31(9)
	R_{wp}	0.067	0.086
	R_p	0.053	0.053
	R_E	0.026	0.021

$$R_{wp} = \{[\sum w(Y_{OBS} - Y_{CAL}/c)^2]/\sum w Y_{OBS}^2\}^{1/2}$$

$$R_p = \sum |Y_{OBS} - Y_{CAL}/c|/\sum Y_{OBS}$$

$$R_E = [(N - P)/\sum w Y_{OBS}^2]^{1/2}$$

^a B (\AA^2) = $8\pi^2\langle\mu^2\rangle$ where $\langle\mu^2\rangle$ is the mean-square amplitude of vibration.

Table 3. Selected Interatomic Distances and Angles for $\text{La}_{0.92}\text{TiO}_3$ and $\text{La}_{0.88}\text{TiO}_3$

bond	multiplicity	$\text{La}_{0.92}\text{TiO}_3$ dist (\AA)	$\text{La}_{0.88}\text{TiO}_3$ dist (\AA)
La-O1	1×	3.121(6)	2.991(9)
La-O1	1×	2.572(7)	2.603(9)
La-O1	1×	3.22(1)	3.046(13)
La-O1	1×	2.417(10)	2.549(13)
La-O2	2×	2.672(5)	2.670(8)
La-O2	2×	2.779(5)	2.806(7)
La-O2	2×	3.358(5)	3.273(6)
La-O2	2×	2.469(6)	2.470(8)
Ti-O1	2×	2.033(2)	1.9887(13)
Ti-O2	2×	2.009(6)	2.038(9)
Ti-O2	2×	2.039(5)	1.98(1)

bonds	angle (deg)	angle (deg)
La-O2-La	97.78(23)	99.2(3)
O1-La-O2	130.98(16)	127.9(3)
Ti-O1-Ti	153.31(45)	164.5(5)
Ti-O2-Ti	156.21(23)	157.0(3)
O1-Ti-O1	180.0(0)	180.0(0)
O2-Ti-O2	180.0(0)	180.0(0)
O1-Ti-O2	89.15(26)	86.8(5)
	90.85(26)	93.4(5)
	88.88(33)	86.4(4)

$b \approx \sqrt{2}a_c$ and $c \approx 2a_c$ where a_c is an idealized cubic perovskite cell of about 3.8 \AA .

From the appearance of the powder patterns it was clear that at least three different orthorhombic symmetries were involved. $\text{La}_{0.92}\text{TiO}_3$ and $\text{La}_{0.88}\text{TiO}_3$ data showed extinctions consistent with $Pbnm$ the space group of one end member, LaTiO_3 . The compositions $\text{La}_{0.80}\text{TiO}_3$ and $\text{La}_{0.75}\text{TiO}_3$ have distinctly simpler patterns consistent with an I-centered cell. $\text{La}_{0.67}\text{TiO}_3$ and $\text{La}_{0.70}\text{TiO}_3$ show several lines which violate $Pbnm$ and I-centering extinctions.

Neutron powder data for $x = 0.08$ ($\text{La}_{0.92}$) and $x = 0.12$ ($\text{La}_{0.88}$) were refined successfully in $Pbnm$ ($Pnma$) and the results are presented in Table 2 for the standard $Pnma$ setting. Selected interatomic distances and angles are listed in Table 3.

Table 4. Atomic and Thermal Parameters Refined from Neutron Powder Data for $\text{La}_{0.80}\text{TiO}_3$ and $\text{La}_{0.75}\text{TiO}_3$ and from Single-Crystal X-ray Data for $\text{La}_{0.75}\text{TiO}_3$ in $Imma^a$

		neutron		X-ray
		$\text{La}_{0.80}\text{TiO}_3$	$\text{La}_{0.75}\text{TiO}_3$	$\text{La}_{0.75}\text{TiO}_3$
La	<i>x</i>	0	0	0
	<i>y</i>	$1/4$	$1/4$	$1/4$
	<i>z</i>	0.9819(24)	0.9813(5)	0.9961(1)
	<i>B</i> (\AA^2)	0.36(9)	0.66(5)	0.0076(1)
Ti	OCC	0.80(1)	0.75(1)	0.7761(2)
	<i>x</i>	$1/2$	$1/2$	$1/2$
	<i>y</i>	0	0	0
	<i>z</i>	0	0	0
O1	<i>B</i> (\AA^2)	0.92(1)	0.47(6)	0.0061(2)
	<i>x</i>	$1/2$	$1/2$	$1/2$
	<i>y</i>	$1/4$	$1/4$	$1/4$
	<i>z</i>	0.0527(24)	0.0409(5)	0.0126(15)
O2	<i>B</i> (\AA^2)	3.05(34)	1.31(7)	0.0326(59)
	<i>x</i>	$1/4$	$1/4$	$1/4$
	<i>y</i>	0.0265(9)	0.0020(14)	-0.0121(10)
	<i>z</i>	$3/4$	$3/4$	$3/4$
	<i>B</i> (\AA^2)	0.93(10)	1.83(4)	0.0357(33)
	R_p	0.0584	0.0565	$[I > 2\sigma(I)]$ $R1 = 0.0347$, $wR2 = 0.0552$
	R_{wp}	0.0630	0.0747	[all I] $R1 = 0.0681$, $wR2 = 0.0070$
	R_E	0.0200	0.0288	GOF 1.34

$$R1 = (\sum ||F_o| - |F_c||/\sum |F_o|)$$

$$wR2 = [\sum w(F_o^2 - F_c^2)^2/\sum w(F_o^2)^2]^{1/2}$$

$$GOF = [\sum w(F_o^2 - F_c^2)^2/(n - p)]^{1/2}$$

^a U_{eq} is defined as one-third of the trace of the orthogonalized U_{ij} tensor.

Table 5. Selected Interatomic Distances and Angles for $\text{La}_{0.80}\text{TiO}_3$ and $\text{La}_{0.75}\text{TiO}_3$

bond	multiplicity	distance (\AA)		
		$\text{La}_{0.80}\text{TiO}_3$ (N)	$\text{La}_{0.75}\text{TiO}_3$ (N)	$\text{La}_{0.75}\text{TiO}_3$ (X)
La-O1	2×	2.7836(16)	2.778(3)	2.7720(6)
La-O1	1×	2.572(19)	2.64(3)	2.716(8)
La-O1	1×	3.155(19)	2.88(3)	2.812(8)
La-O2	4×	2.680(9)	2.719(8)	2.689(5)
La-O2	4×	2.873(8)	2.800(8)	2.797(6)
Ti-O1	2×	1.9781(21)	1.963(3)	1.9495(4)
Ti-O2	4×	1.9697(9)	1.9501(3)	1.951(1)

bond	angle (deg)	angle (deg)	angle (deg)
La-O2-La	86.69(20)	87.4(3)	89.3(1)
O1-La-O1	172.1(7)	117.99(10)	119.0(1)
Ti-O1-Ti	163.1(8)	166.80(16)	175.9(5)
Ti-O2-Ti	167.9(4)	179.1(6)	174.6(5)
O1-Ti-O1	180.0(0)	180.0(0)	180.0(1)
O2-Ti-O2	180.0(0)	180.0(0)	180.0(1)
O1-Ti-O2	90.00(3)	95.1(3)	94.2(3)
	90.00(3)	84.9(3)	85.8(3)

Refinement of both the $\text{La}_{0.80}\text{TiO}_3$ and $\text{La}_{0.75}\text{TiO}_3$ neutron data was successful in $Ibmm$ ($Imma$), the same space group found for intermediate compositions in the $\text{La}_{1-x}\text{Sr}_x\text{TiO}_3$ series and the results are shown in Table 4. Again, lists of interatomic distances and angles are found in Table 5.

A single-crystal sample of $\text{La}_{0.75}\text{TiO}_3$ was available and X-ray single-crystal data were also consistent with the $Ibmm$ model as also shown in Table 4.

The structure determination for $\text{La}_{0.67}\text{TiO}_3$ was less straightforward. X-ray data collected on the apparent single crystals of $\text{La}_{0.67}\text{TiO}_3$ obtained from the flux growth gave a unit cell somewhat different from that from the Guinier camera data on either the powder or ground single-crystal sample (Table 1), $a = b = 5.485$ (10) \AA , $c = 7.749$ (2) \AA with Ag $K\alpha$ ($\lambda = 0.56086$ \AA)

Table 6. Positional Parameters for La_{0.67}TiO₃ from Single-Crystal X-ray Data in *Pmmn*

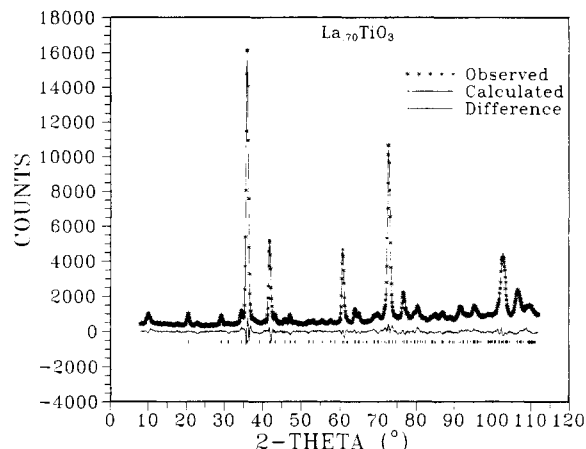
	<i>x</i>	<i>y</i>	<i>z</i>
La1	1/4	-0.5048(5)	1/4
La2	1/4	0.0027(3)	1/4
Ti1	1/4	0.2586(7)	3/4
Ti2	1/4	-0.2498(8)	3/4
O1	0.0140(6)	-0.2432(6)	-0.5168(7)
O2	1/4	0.0012(43)	3/4
O3	1/4	0.5028(41)	3/4

Table 7. Positional and Thermal Parameters for La_{0.67}TiO₃ and La_{0.70}TiO₃ from Powder Neutron Diffraction Data and from X-ray Single-Crystal Data for La_{0.67}TiO₃ in *Pban*

	neutron		X-ray	
	La _{0.67} TiO ₃	La _{0.70} TiO ₃	La _{0.67} TiO ₃	
La1 <i>x</i>	1/4	1/4	1/4	
<i>y</i>	1/4	1/4	1/4	
<i>z</i>	0	0	0	
<i>B</i> (Å ²)	0.64(11)	0.32(7)	<i>U</i> _{eq}	0.00645(9)
occ	1.00(1)	1.00(1)		0.820(1)
La2 <i>x</i>	1/4	1/4	1/4	
<i>y</i>	1/4	1/4	1/4	
<i>z</i>	1/2	1/2	1/2	
<i>B</i> (Å ²)	1.20(36)	0.67(22)	<i>U</i> _{eq}	0.00645(9)
occ	0.335(1)	0.40(1)		0.515(2)
Ti <i>x</i>	1/4	1/4	1/4	
<i>y</i>	3/4	3/4	3/4	
<i>z</i>	0.2608(20)	0.2596(12)	<i>U</i> _{eq}	0.2545(1)
<i>B</i> (Å ²)	0.69(14)	0.25(10)		0.00560(10)
O1 <i>x</i>	-0.0137(38)	-0.0200(22)		-0.01558(60)
<i>y</i>	-0.0207(23)	-0.0225(14)		-0.01591(58)
<i>z</i>	0.2431(7)	0.2417(6)		0.24420(59)
<i>B</i> (Å ²)	0.45(7)	0.73(8)	<i>U</i> _{eq}	0.01541(63)
O2 <i>x</i>	3/4	3/4	3/4	
<i>y</i>	1/4	1/4	1/4	
<i>z</i>	1/2	1/2	1/2	
<i>B</i> (Å ²)	3.53(33)	2.18(26)	<i>U</i> _{eq}	0.02850(195)
occ				
O3 <i>x</i>	3/4	3/4	3/4	
<i>y</i>	1/4	1/4	1/4	
<i>z</i>	0	0	0	
<i>B</i> (Å ²)	2.46(28)	0.62(19)	<i>U</i> _{eq}	0.02776(186)
<i>R</i> _p	0.0651	0.0570	[<i>I</i> > 2δ(<i>I</i>)]	<i>R</i> ₁ = 0.0539, <i>wR</i> = 0.1152
<i>R</i> _{wp}	0.0806	0.0745	[all <i>I</i>]	<i>R</i> ₁ = 0.0883, <i>wR</i> ₂ = 0.1272 = 1.338
<i>R</i> _E	0.0326	0.0300	GOF	
<i>S</i>	2.47	2.49		

radiation. Examination of systematic absences suggested the possible space group *Pban*, but about 30 very weak reflections violated the *b* and *a* glide plane extinctions. A first solution was thus attempted in *Pmmn*, but the results were not satisfactory. Although the refinement converged with residuals *R*₁ = 0.0507, *wR*₂ = 0.0801 and goodness-of-fit = 2.26, inspection of refined parameters in *Pmmn* (or *Pmnm*) shown in Table 6 indicates that the *y* coordinates for La1, La2, O2, and O3 are very near special positions. In addition the two Ti positions were very highly correlated in the refinement, indicating that there is really only one Ti site. These observations raise the possibility that the La_{0.67}TiO₃ crystal is merohedrally twinned or that the weak reflections arise from some other effect such as multiple scattering.

As the powder neutron data would not be effected by twinning, attempts were made to refine the structure by the Rietveld method in both *Pmmn* and *Pban*. Similar to the X-ray results, the *Pmnm* model could not be refined without constraining the thermal parameters of the pairs La1, La2 and Ti1, Ti2. In addition the positional parameters of the two Ti sites were 90%

**Figure 3.** Neutron powder profile data for La_{0.70}TiO₃ refined in *Pban*.**Table 8. Selected Interatomic Distances and Angles for La_{0.67}TiO₃ and La_{0.70}TiO₃ from Powder Neutron Data and for La_{0.67}TiO₃ from X-ray Diffraction Data**

bond	multiplicity	distance (Å)		
		La _{0.67} TiO ₃ (N)	La _{0.70} TiO ₃ (N)	La _{0.67} TiO ₃ (<i>x</i>) ^a
La1-O1	4×	2.607(13)	2.576(10)	2.622(4)
La1-O1	4×	2.797(13)	2.825(11)	2.796(4)
La1-O3	2×	2.728(2)	2.7374(22)	2.730(2)
La1-O3	2×	2.738(2)	2.7455(15)	2.738(4)
La2-O1	4×	2.871(13)	2.916(10)	2.858(4)
La2-O1	4×	2.686(12)	2.676(10)	2.688(4)
La2-O2	2×	2.728(2)	2.7374(22)	2.730(20)
La2-O2	2×	2.738(2)	2.7455(15)	2.739(14)
T-O1	2×	1.913(18)	1.938(14)	1.937(3)
Ti-O1	2×	1.969(17)	1.969(13)	1.941(3)
Ti-O2	1×	1.856(16)	1.846(11)	1.906(1)
Ti-O3	1×	2.024(16)	2.041(11)	1.975(1)

bonds	angle (deg)	angle (deg)	angle (deg)
Ti-O1-Ti	168.7(9)	165.9(7)	171.39(20)
Ti-O2-Ti	180.0	180.0	180.0
Ti-O3-Ti	180.0	180.0	180.0
O2-Ti-O3	180.0	180.0	180.0
O1-Ti-O1	89.8(7)	89.6(6)	89.74(03)
O1-Ti-O1	171.8(10)	170.4(7)	175.29(28)
O1-Ti-O2	94.1(5)	94.8(4)	92.35(14)
O1-Ti-O3	86.0(8)	85.2(4)	87.64(14)

^a The cell constants determined from the Guinier X-ray data were used to determine interatomic distances in this case.

correlated. On the other hand refinement in *Pban* proceeded smoothly to the results presented in Table 7. The slightly high residuals result from the presence of a small amount of a second phase as mentioned. Somewhat better results for La_{0.70}TiO₃ which is a single-phase sample were obtained, also in *Pban*, and these are listed as well in Table 7. Figure 3 shows the profile fit for La_{0.70}TiO₃. Table 8 lists selected bond distances and angles.

Returning to the X-ray single-crystal data, a refinement was then carried out in *Pban* by excluding the weak reflections. This refinement converged to residuals which are identical, essentially, with those obtained for *Pmmn* but with 13 fewer parameters, *R*₁ = 0.0539, *wR*₂ = 0.1152, GOF = 1.338. The details of the single-crystal refinements for La_{0.67} and La_{0.75} are listed in Table 9. The smaller esd's for all parameters in the X-ray refinement indicate that these results are more accurate than those determined from the neutron powder data. In all but two cases, the derived bond

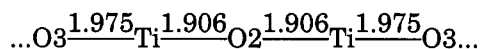
Table 9. Crystal Data for $\text{La}_{0.67}\text{TiO}_3$ and $\text{La}_{0.75}\text{TiO}_3$

	$\text{La}_{0.75}\text{TiO}_3$	$\text{La}_{0.67}\text{TiO}_3$
color, habit	black, plate	transparent yellow, rectangular prism
crystal size (mm)	$0.2 \times 0.2 \times 0.1$	$0.15 \times 0.15 \times 0.25$
crystal system	orthorhombic	orthorhombic
space group	<i>Imma</i>	<i>Pban</i>
unit-cell dimensions	$a = 5.5130(10) \text{ \AA}$ $b = 7.712(2) \text{ \AA}$ $c = 5.5130(10) \text{ \AA}$	$a = 5.4850(10) \text{ \AA}$ $b = 5.4850(10) \text{ \AA}$ $c = 7.749(2) \text{ \AA}$
volume	$234.39(9) \text{ \AA}^3$	$233.13(9) \text{ \AA}^3$
Z	4	4
formula weight	203.8	188.5
density (calc)	5.775 Mg/m^3	5.370 Mg/m^3
absorption coefficient	17.125 mm^{-1}	15.254 mm^{-1}
$F(000)$	361.08	335.98
diffractometer used	Siemens 3	Siemens 3
radiation	Ag K α ($\lambda = 0.56086 \text{ \AA}$)	Ag K α ($\lambda = 0.56086 \text{ \AA}$)
temp (K)	298	298
monochromator	highly oriented graphite crystal	highly oriented graphite crystal
2θ range	$3.0\text{--}80.0^\circ$	$4.14\text{--}75.22^\circ$
scan type	$2\theta\text{--}\theta$	$2\theta\text{--}\theta$
scan speed	variable, $1.50\text{--}14.00^\circ/\text{min}$ in ω	variable, $1.50\text{--}14.00^\circ/\text{min}$ in ω
scan range (ω)	1.00° plus K α separation	1.00° plus K α separation
background measurement	stationary crystal and stationary counter at beginning and end of scan, each for 25.0% of total scan time	stationary crystal and stationary counter at beginning and end of scan, each for 25.0% of total scan time
standard reflections	3 measured every 97 reflections	3 measured every 97 reflections
index ranges	$-9 \leq h \leq 9, -19 \leq k \leq 19, 0 \leq l \leq 13$	$0 \leq h \leq 11, -11 \leq k \leq 11, -16 \leq l \leq 16$
reflections collected	2149	4753
independent reflections	617 ($R_{\text{int}} = 4.73\%$)	1263 ($R_{\text{int}} = 3.31\%$)
absorption correction	DIFABS	DIFABS
data/restraints/parameters	617/0/19	1263/0/28
largest diff peak and hole	1.90 and -2.43 e \AA^{-3}	3.21 and -2.49 e \AA^{-3}

distances for the neutron powder and single-crystal derived values agree to within one or two times the esd's as seen in Table 8.

Figures 4 and 5 give two views of the three structure types observed in the $\text{La}_{1-x}\text{TiO}_3$ system. All three involve networks of corner sharing Ti–O octahedra with La^{3+} ions and vacancies occupying the interstitial space.

The *Pban* structure is apparently a novel perovskite type and will be discussed first. In this structure the La^{3+} ions occupy the La1 ($z = 0$) site preferentially at the rate of 82%, leaving the La2 site ($z = 1/2$) about half empty. The Ti atoms are displaced from the centers of the octahedra toward the $z = 1/2$ layer perhaps to compensate for the formal cation deficit. This results in linear chains parallel to the c axis as shown here for $\text{La}_{0.67}\text{TiO}_3$:



i.e., with alternating blocks of two short Ti–O bonds and two long Ti–O bonds. The Ti–O–Ti angle is rigorously 180° parallel to c and 171° normal to c . These features are seen clearly in Figure 4c. From a view parallel to the c axis, Figure 5c, it can be seen that adjacent octahedra in the same chain are twisted slightly about the c -axis direction.

The *Ibmm* (*Imma*) and *Pbnm* (*Pnma*) structures are closely related as, indeed, a group–subgroup relationship exists. There is only one La site and the Ti site has a center of symmetry, $2/m$ in *Ibmm* and $\bar{1}$ in *Pbnm*. None of the Ti–O–Ti angles is constrained by symmetry.

The two structure types can be contrasted in terms of Glaser's octahedral tilt scheme for perovskite related structures.²¹ The *Ibmm* space group is consistent with an octahedral tilting pattern involving tilts about two

of three orthogonal subcell axes and *Pbnm* is a three-axis tilt system. Interestingly, the *Pban* structure, evidently a two-axis tilt system, does not appear in Glaser's classification.

Figure 6 illustrates systematic structural trends for $\text{La}_{1-x}\text{TiO}_3$ as a function of x . Note in Figure 6a that the cell volume varies linearly with x with no anomalies at the structural boundaries. This is in sharp contrast to the reported behavior for $\text{La}_{1-x}\text{Sr}_x\text{TiO}_3$ of Figure 1 where a markedly nonlinear dependence on x is seen with clear changes at the structural phase boundaries. Figure 6b,c also indicates that the composition dependence of the average values of the Ti–O distance and Ti–O–Ti angles is also essentially linear. The boundaries given by the vertical lines mark the values of the largest positive and negative excursions from the mean value and are thus some measure of the degree of distortion of the Ti–O octahedra on one hand and the degree of bond angle distribution on the other. The fact that the vertical bars are largest for the *Pban* structure materials reflects the more distorted local Ti–O environment for these compositions relative to the *Pbnm* and *Ibmm* structure types. This information may be useful in correlating structure with physical properties.

One final structural point is that the transition from the *Pban* type to the adjacent *Ibmm* type is not necessarily sharp. This is illustrated in Figure 7 in which the neutron diffraction profile for the (001) reflection is shown for $\text{La}_{0.67}$, $\text{La}_{0.70}$, both *Pban* materials and $\text{La}_{0.75}$ which is best described as *Ibmm*. Nonetheless, there exists a remnant of the (001) reflection which is forbidden of course in *I* symmetry but the reflection is very broad. This may indicate the presence of small domains with a local structure similar to the *Pban* structure within an overall *Ibmm* long-range order.

(21) Glaser, A. M. *Acta Crystallogr.* **1975**, *A31*, 756.

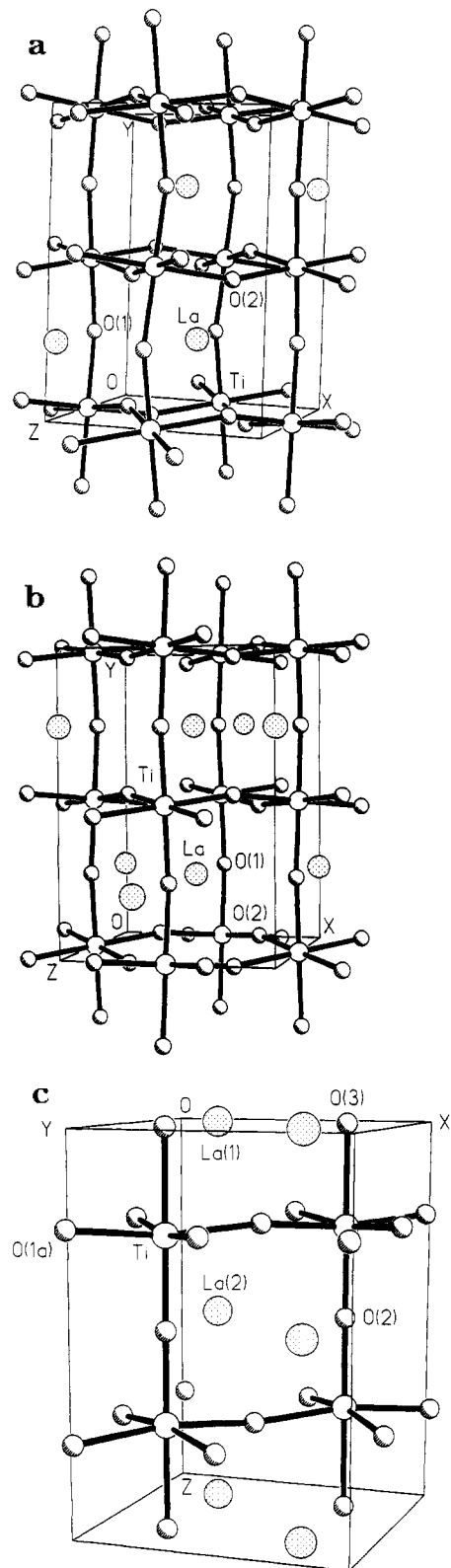


Figure 4. View of the crystal structures of (a) $\text{La}_{0.92}\text{TiO}_3$ ($Pbnm$), (b) $\text{La}_{0.75}\text{TiO}_3$ ($Ibmm$), and (c) $\text{La}_{0.67}\text{TiO}_3$ ($Pbam$), normal to the c axis.

To summarize this section, it has been shown that a solid solution exists between $\text{La}_{2/3}\text{TiO}_3$ and LaTiO_3 and that a description of oxidized forms of LaTiO_3 which retain the orthorhombic perovskite structure is more realistically formulated as $\text{La}_{1-x}\text{TiO}_3$ rather than LaTiO_{3+x} which had been proposed earlier.⁸ Support for this model consists of the direct synthesis and successful structure refinement of various members of

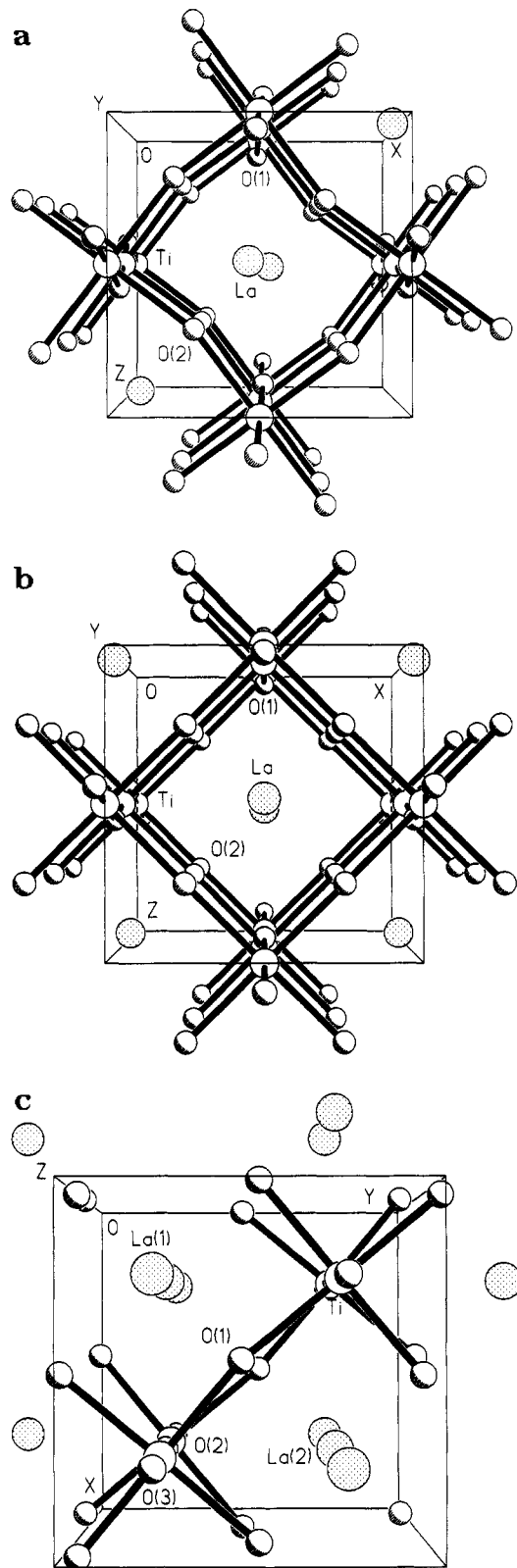


Figure 5. View of the crystal structures of (a) $\text{La}_{0.92}\text{TiO}_3$ ($Pbnm$), (b) $\text{La}_{0.75}\text{TiO}_3$ ($Ibmm$), and (c) $\text{La}_{0.67}\text{TiO}_3$ ($Pbam$), parallel to the c axis.

the series with large concentrations of vacancies on the La^{3+} site. The observed decrease in unit-cell volume as LaTiO_3 is oxidized is also not consistent with an oxide interstitial model. For example, in $\text{La}_2\text{NiO}_{4+y}$ where the presence of oxide interstitials in the rock salt layer of this phase has been verified, the cell volume change between the $y = 0$ phase $379.66(2) \text{ \AA}^3$ and the oxidized

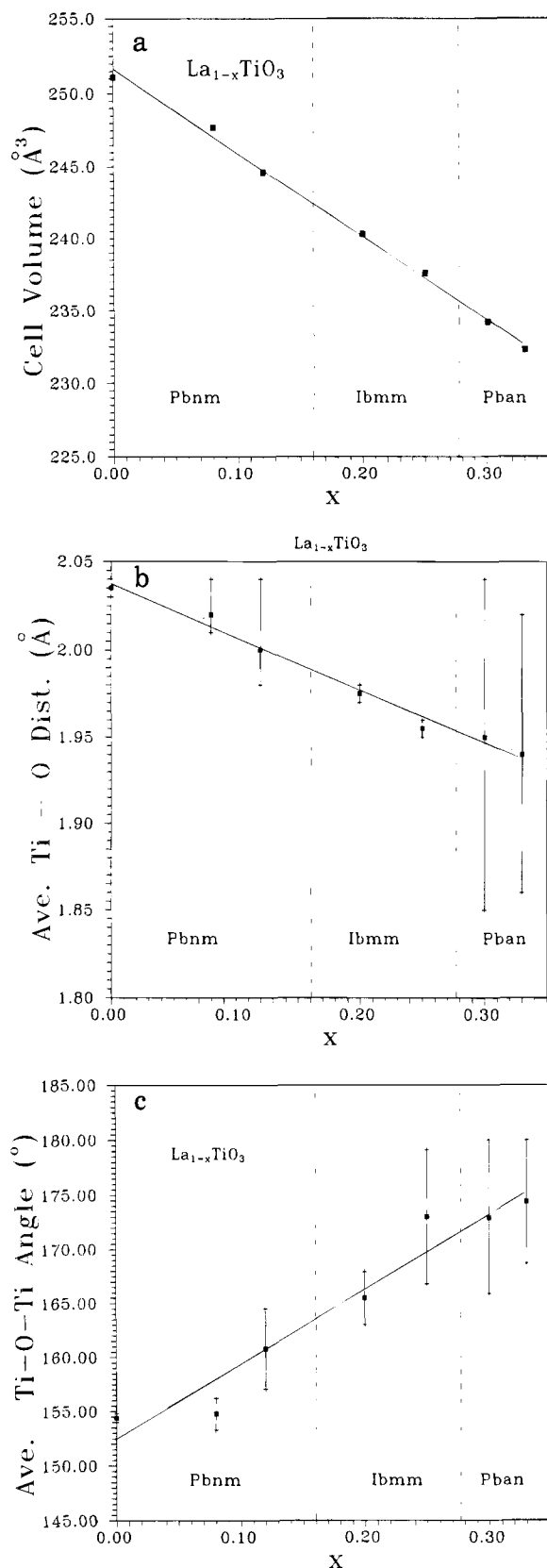


Figure 6. (a) Dependence of the cell volume on x in $\text{La}_{1-x}\text{TiO}_3$. Crystallographic phase boundaries are indicated. (b) Variation of the average Ti-O distance with x in $\text{La}_{1-x}\text{TiO}_3$. The error bars represent the maximum excursions from the average in the coordination octahedron. The neutron powder results are plotted. (c) Variation of the average Ti-O-Ti angle α with x in $\text{La}_{1-x}\text{TiO}_3$. The error bars represent the maximum excursions from the average in the edge links which join the octahedra. The neutron powder results are plotted.

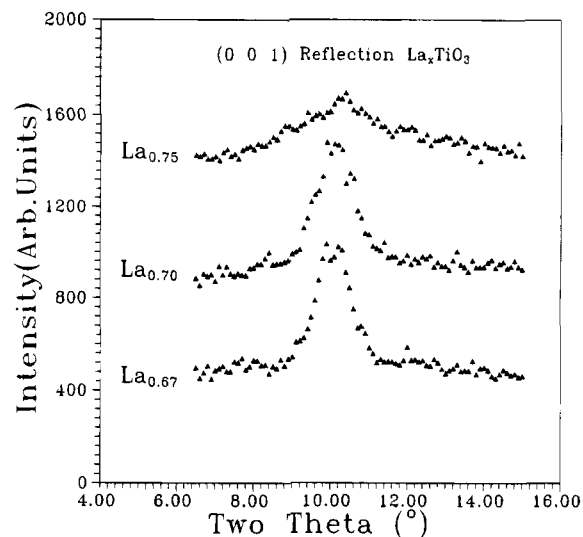


Figure 7. The (001) reflection in $\text{La}_{0.67}\text{TiO}_3$ and $\text{La}_{0.70}\text{TiO}_3$ (*Pban*) and $\text{La}_{0.75}\text{TiO}_3$ (*Ibmm*).

$y = 0.18$ phase $379.96(3) \text{ \AA}^3$ is negligible.²² Of course the observation of interstitials only in the rock salt layer and not in the perovskite layer is further evidence against this description of the LaTiO_{3+x} phases. It should be possible to map the compositions of the LaTiO_{3+x} phases onto the more appropriate $\text{La}_{1-x}\text{TiO}_3$ description by matching observed unit-cell volumes. Unfortunately, accurate cell volumes are not given in ref 8. For only one case, $x = 0.20$, the most oxidized sample studied, were approximate cell constants derived from TEM diffraction data given from which a volume of 242.9 \AA^3 could be deduced. This is intermediate between values appropriate to $\text{La}_{0.80}\text{TiO}_3$ (240.3 \AA^3) and $\text{La}_{0.88}\text{TiO}_3$ (244.6 \AA^3) indicating a probable composition of $\text{La}_{0.84}\text{TiO}_3$.

Results from this section also indicate that the single-crystal materials for which electrical transport and optical conductivity studies have been reported in a companion paper¹¹ are indeed correctly identified as $\text{La}_{0.88}\text{TiO}_3$, sample D, and $\text{La}_{0.92}\text{TiO}_3$, sample C, by the close matching of their cell volumes, 244.7 \AA^3 for sample D and 244.6 \AA^3 for $\text{La}_{0.88}\text{TiO}_3$ and 247.8 \AA^3 for sample C and 247.7 \AA^3 for $\text{La}_{0.92}\text{TiO}_3$.

Finally, the structure of $\text{La}_{2/3}\text{TiO}_3$ has been determined for the first time, nearly 40 years after the compound was first reported and is, apparently, a new perovskite structure type described in *Pban*.

Physical Properties. Resistivity. The electrical resistivity of five of the six compositions studied here is shown in Figure 8 over the temperature range 5–300 K. $\text{La}_{2/3}\text{TiO}_3$ is an insulator. There is a clear progression from insulating to metallic behavior as $\text{La}_{2/3}\text{TiO}_3$ is reduced. $\text{La}_{0.70}\text{TiO}_3$ is semiconducting with a room-temperature resistivity of $3.2 \text{ } \Omega \text{ cm}$ at 300 K rising to $93 \text{ } \Omega \text{ cm}$ at 5 K. On a linear scale the resistivity temperature dependence is sigmoidal in shape and plots of $\log \rho$ vs T^{-1} are distinctly nonlinear over the range 150–300 K, so an activation energy cannot be determined. Plots of $\log \sigma$ vs $T^{-1/4}$ were constructed²³ and are also nonlinear over this range. Such a dependence

(22) Jorgensen, J. S.; Dabrowski, B.; Pei, S.; Richards, D. R.; Hinks, D. G. *Phys. Rev.* **1989**, *B40*, 2187.

(23) Taguchi, Y.; Tokura, Y.; Arima, T.; Inaba, F. *Phys. Rev.* **1993**, *B48*, 511.

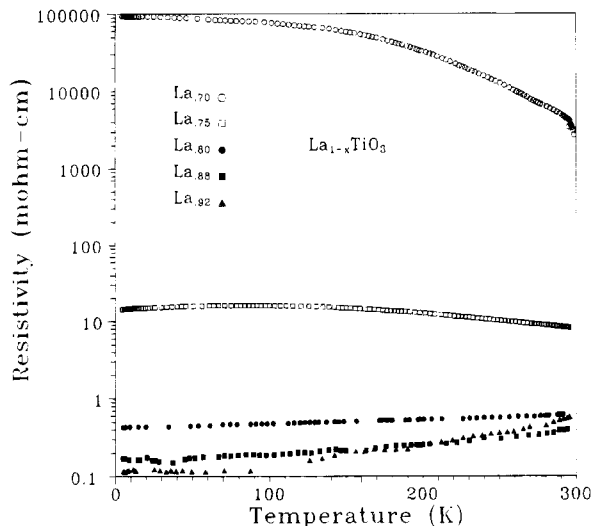


Figure 8. Temperature variation of the resistivity for several compositions in $\text{La}_{1-x}\text{TiO}_3$.

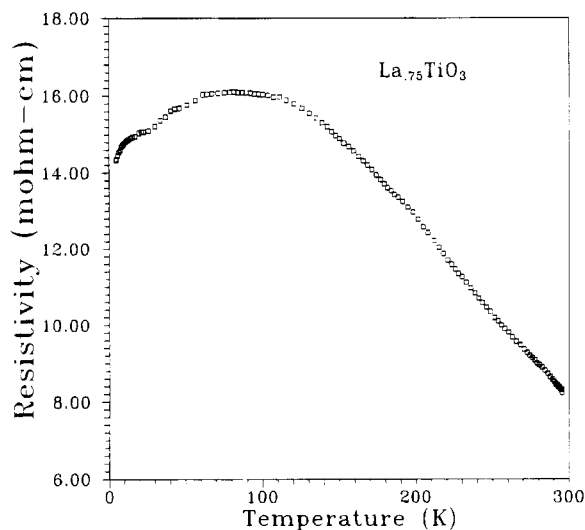


Figure 9. Temperature variation of the resistivity for $\text{La}_{0.75}\text{TiO}_3$.

which is characteristic of variable range hopping might have been expected given the high disorder levels in this system. The results for $\text{La}_{0.75}\text{TiO}_3$ are even more remarkable on a linear scale as shown in Figure 9 where a broad semiconductor-to-metal transition is apparent, beginning slightly above 100 K. The data in the range $150 \text{ K} < T < 300 \text{ K}$ were analyzed by plotting $\ln \sigma$ versus both T^{-1} and $T^{-1/4}$. In each case the data separate into two reasonably linear regions, $160 \text{ K} < T < 200 \text{ K}$ and $210 \text{ K} < T < 290 \text{ K}$ as seen in Figure 10 where the $T^{-1/4}$ plot is shown. Although fits to both models give reasonable results, the fit to the $T^{-1/4}$ law is significantly better for both temperature ranges. This can be seen by comparing the relative statistical uncertainties for the derived slopes as determined from $\ln \sigma = AT^n + B$. For the range $160 \text{ K} < T < 200 \text{ K}$, $A = 98(2)$ for $n = -1$, an error of 2.04% and $A = 8.0(1)$ for $n = -1/4$, an error of 1.25%. For the range $210 \text{ K} < T < 290 \text{ K}$, $A = 273(4)$ with $n = -1$, an error of 1.47%, and $A = 1.76(2)$ with $n = -1/4$, an error of 1.14%. While not conclusive, this observation suggests strongly that disorder-induced localization may play a role in the localization mechanism in $\text{La}_{0.75}\text{TiO}_3$.

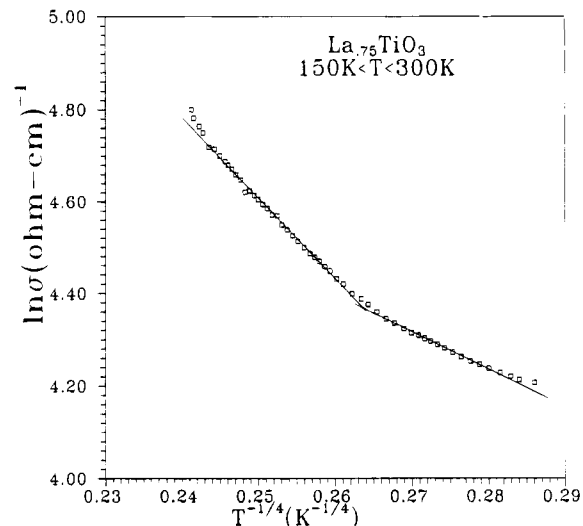


Figure 10. Conductivity data in the range $150 < T < 300 \text{ K}$ for $\text{La}_{0.75}\text{TiO}_3$ analysed in terms of $\ln \sigma = AT^{-1/4} + B$, i.e., a variable range hopping model. Fitting constants for the two ranges are $160 \text{ K} < T < 200 \text{ K}$, $A = 8.0(1)$, $B = 6.490(2)$, and $210 \text{ K} < T < 290 \text{ K}$, $A = 17.6(2)$, $B = 9.01(1)$.

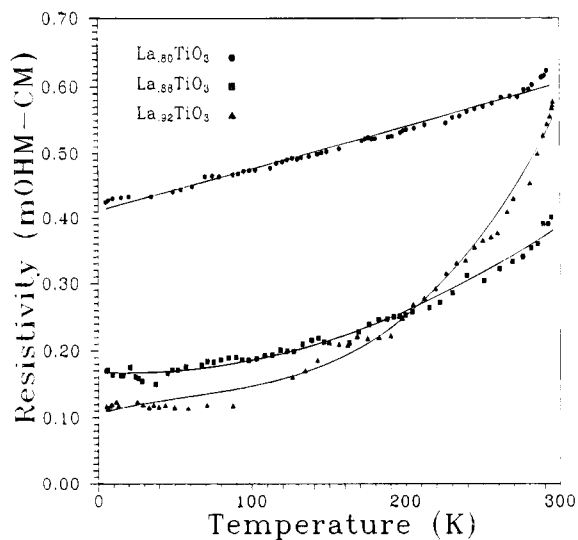


Figure 11. Temperature variation of the resistivity for the metallic compositions in $\text{La}_{1-x}\text{TiO}_3$. The solid lines are guides to the eye.

It is worth noting that the shapes of the resistivity curves for $\text{La}_{0.70}$ and $\text{La}_{0.75}$ resemble those found near the metal-insulator transition in the related perovskite system $\text{Y}_{1-x}\text{Ca}_x\text{TiO}_3$.²⁴ For the remaining compositions the resistivity drops to room-temperature values of less than $10^{-3} \Omega \text{ cm}$ and true metallic behavior is seen as evident from Figure 11. Note the nearly linear dependence for $\text{La}_{0.80}\text{TiO}_3$. The behavior of the remaining two compositions is quantitatively similar to that of the single-crystal materials of the same composition described in ref 11.

The electrical properties of the $\text{La}_{1-x}\text{TiO}_3$ series are shown qualitatively in Figure 12 as a function of Ti^{3+} concentration and can be compared with those for $\text{La}_{1-x}\text{Sr}_x\text{TiO}_3$, Figure 2. Note the much broader insulating range for small concentrations which exists out to about 24% Ti^{3+} for the $\text{La}_{1-x}\text{TiO}_3$ series while cor-

(24) Mott, N. F.; Davis, E. A. *Electronic Processes in Non-Crystalline Materials*; Clarendon Press: New York, 1971; p 42.

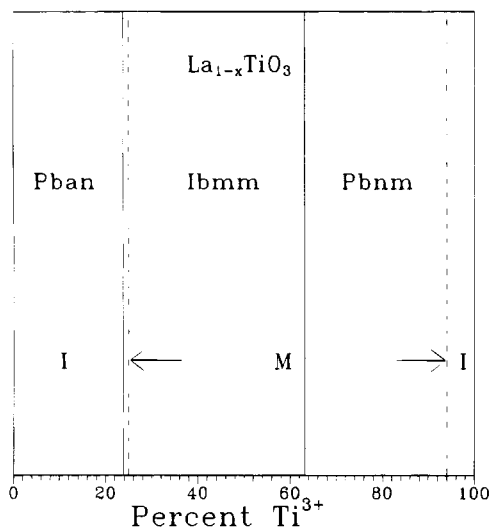


Figure 12. Comparison of the crystal structure and electrical properties as a function of Ti^{3+} concentration in $\text{La}_{1-x}\text{TiO}_3$. The solid vertical lines separate regions of different crystal structure and the dashed lines regions of I (insulating) or M (metallic) behavior.

responding materials are metallic in $\text{La}_{1-x}\text{Sr}_x\text{TiO}_3$. There is much closer agreement for large Ti^{3+} concentrations. The transition from insulating to metallic character seems to correlate well with the position of the *Pban/Ibmm* boundary in $\text{La}_{1-x}\text{TiO}_3$ while there is no change at the *Pm3m/Ibmm* boundary in the Sr-doped series. These differences can be understood in terms of the singular structure of the *Pban* phase which, as pointed out earlier, involves linear chains along the *c* axis which are characterized by alternating blocks of two short Ti–O distances and two long Ti–O distances. It is reasonable that electrons could be trapped in the blocks with the short Ti–O distances, forming in effect dimers, through the shared oxygen atom. It is more difficult to envisage trapping in the cubic *Pm3m* structure which pertains for the $\text{La}_{1-x}\text{Sr}_x\text{TiO}_3$ system over the same range of Ti^{3+} concentration. In addition, the perturbation on the periodic potential seen by the d electrons may be greater for the large *x* region of the $\text{La}_{1-x}\text{TiO}_3$ series due to the high concentration of La^{3+} vacancies. Thus, there may be a component of Anderson-type localization to consider as well.²⁵

Our results differ from those of Bazuev et al.,¹⁶ who have reported that $\text{La}_{0.70}\text{TiO}_3$ is metallic but are in general agreement regarding the metallic behavior of $\text{La}_{0.80}\text{TiO}_3$ and $\text{La}_{0.90}\text{TiO}_3$.

The presence of a T^2 term in the resistivity data for $\text{La}_{0.88}$ and $\text{La}_{0.92}$ was tested by fitting to the expression, $\rho = \rho_0 + AT^2$. A reasonable fit was found over nearly the entire range studied as seen in Figure 13 with the parameters listed in Table 10. A T^2 term is normally ascribed to a strong electron–electron scattering process and the coefficient, *A*, can be taken as a relative measure of the extent of correlation in the system. Such a T^2 term was also found in the $\text{La}_{1-x}\text{Sr}_x\text{TiO}_3$ series and the *A* increased systematically with decreasing *x* or increasing Ti^{3+} content.⁴ The *A* values found in the $\text{La}_{1-x}\text{TiO}_3$ system are significantly larger than those found in $\text{La}_{1-x}\text{Sr}_x\text{TiO}_3$ for comparable Ti^{3+} concentra-

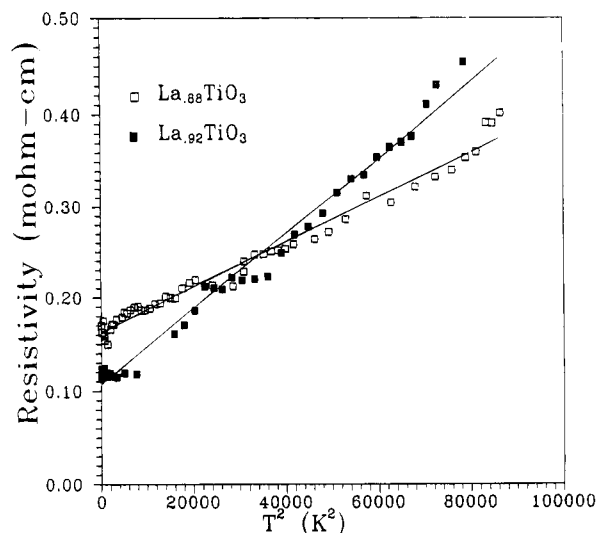


Figure 13. Resistivity data for $\text{La}_{0.88}\text{TiO}_3$ and $\text{La}_{0.92}\text{TiO}_3$ plotted versus T^2 . The solid lines are least squares fits to the function $\rho = \rho_0 + AT^2$ and the derived values are listed in Table 11.

Table 10. Comparison of Parameters Derived from a Fit of $\rho = \rho_0 + AT^2$ for $\text{La}_{1-x}\text{TiO}_3$ and $\text{La}_{1-x}\text{Sr}_x\text{TiO}_3$

composition	Ti^{3+}	<i>A</i> ($\Omega \text{ cm K}^{-2} \times 10^9$)	ρ_0 ($\Omega \text{ cm}$)
$\text{La}_{0.88}\text{TiO}_3$	63%	2.47	1.63×10^{-4}
$\text{La}_{0.92}\text{TiO}_3$	75%	4.08	1.07×10^{-4}
$\text{La}_{0.70}\text{Sr}_{0.30}\text{TiO}_3$	70%	1.00	
$\text{La}_{0.80}\text{Sr}_{0.20}\text{TiO}_3$	80%	1.21	
$\text{La}_{0.90}\text{SrTiO}_3$	90%	1.50	
$\text{La}_{0.95}\text{Sr}_{0.05}\text{TiO}_3$	95%	2.50	

tions as seen in Table 10, suggesting greater levels of correlation or localization in the former.

Magnetic susceptibility data corrected for core diamagnetism are shown for each composition studied in Figure 14. All have roughly the same behavior consisting of a low-temperature Curie–Weiss tail and a largely temperature-independent susceptibility over most of the range up to 300 K. The data could be fit well to a Curie–Weiss plus TIP term:

$$\chi_m = \frac{C}{T - \theta} + \chi_{\text{TIP}}$$

and the fitted values are collected in Table 11.

The *C* and θ values are very small, especially the former when compared to the free ion value of $0.37 \text{ cm}^3/\text{mol}$ of Ti^{3+} . For example, *C* for the $\text{La}_{0.70}\text{TiO}_3$ phase which has formally 9% Ti^{3+} is only a factor of 0.078 of the expected *C* value assuming free ion behavior for the Ti^{3+} spins. This is perhaps further reason to believe that there exists significant spin pairing in this compound as postulated earlier in the context of the insulating transport properties. $\text{La}_{0.70}\text{TiO}_3$ also shows a very large χ_{TIP} value which must, presumably, be of the van Vleck type as there are few free carriers.

Much smaller χ_{TIP} values are seen for the metallic phases and the metal/semiconductor material $\text{La}_{0.75}\text{TiO}_3$. These values which are on the order of $2 \times 10^{-4} \text{ cm}^3 \text{ mol}^{-1}$ are still very large in comparison to those found for the tungsten bronzes, e.g., Na_xWO_3 , of similar carrier density which are on the order of $0.15 \times 10^{-4} \text{ cm}^3 \text{ mol}^{-1}$.²⁶ These latter materials are thought

(25) Anderson, P. W. *Phys. Rev.* **1958**, *109*, 1992; *Commun. Solid State Phys.* **1970**, *2*, 193. See also ref 24, p 16.

(26) Kupka, F.; Sienko, M. J. *J. Chem. Phys.* **1950**, *18*, 1296.

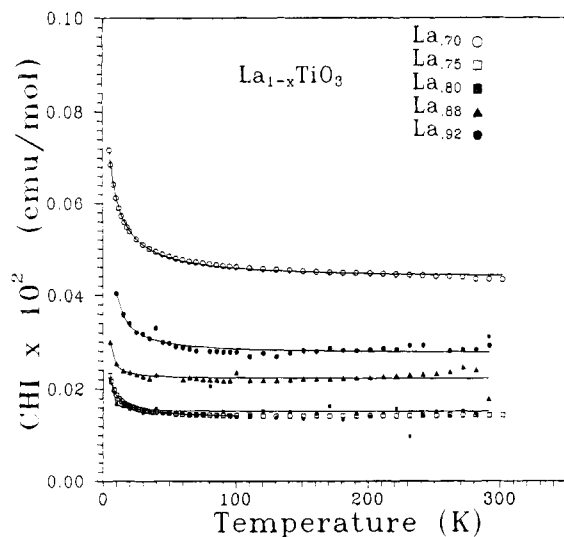


Figure 14. Magnetic susceptibilities for $\text{La}_{1-x}\text{TiO}_3$. The solid lines are fits to $\chi = (C/T - \theta) + \chi_{\text{TIP}}$ and the derived parameters are listed in Table 10.

Table 11. Values of C , θ , and χ_{TIP} from the Magnetic Susceptibilities of $\text{La}_{1-x}\text{TiO}_3$

x	C ($\text{cm}^3 \text{K/mol}$)	θ (K)	χ_{TIP} ($\text{cm}^3 \text{mol}^{-1}$)
0.30	2.6×10^{-3}	-4.2	4.34×10^{-4}
0.25	5.2×10^{-4}	-0.7	1.30×10^{-4}
0.20	1.0×10^{-4}	+3.5	1.52×10^{-4}
0.12	2.1×10^{-4}	+2.4	2.22×10^{-4}
0.08	1.1×10^{-3}	+1.6	2.75×10^{-4}

to be good examples of nearly free electron systems with $m^*/m_c \approx 2$ or less. This implies a large m^*/m ratio for the $\text{La}_{1-x}\text{TiO}_3$ series.

There are three contributions to the χ_{TIP} term, apart from the core diamagnetism, a van Vleck type which is paramagnetic and both a diamagnetic and paramagnetic contribution from the carriers given in the simplest approximation as

$$\chi = \frac{4m^*\mu_B^2}{h^2}(3\pi^2n)^{1/3}\left(1 - \frac{m_0^2}{3m^{*2}}\right)$$

where h is Planck's constant, n the carrier density, and m and m^* the rest and effective mass of the electron. As the m/m^* ratio is likely to be small, only the paramagnetic term is important. There exists no obvious way to separate these components, and no attempts will be made here, but it is most likely that the carrier-concentration term is dominant and that has been assumed in the analysis of corresponding susceptibility results for $\text{La}_{1-x}\text{Sr}_x\text{TiO}_3$.

The χ_{TIP} values of Table 10 are plotted along with those for $\text{La}_{1-x}\text{Sr}_x\text{TiO}_3$ from two sources and with $\text{SrTiO}_{2.72}$ in Figure 15 as a function of Ti^{3+} concentration. First note that the χ_{TIP} values for $\text{La}_{1-x}\text{Sr}_x\text{TiO}_3$ increase monotonically with increasing Ti^{3+} content, the solid and dashed lines in the figure. The results from ref 1 show somewhat more scatter and lie consistently below those of ref 4, presumably due to the fact that the former data have not been corrected for core diamagnetism. With this correction of about $(50-60) \times 10^{-6} \text{ cm}^3 \text{ mol}^{-1}$, the two data sets would agree reasonably well.

Second, the data for $\text{La}_{1-x}\text{TiO}_3$ deviate strongly from the trend for $\text{La}_{1-x}\text{Sr}_x\text{TiO}_3$ for low Ti^{3+} concentrations

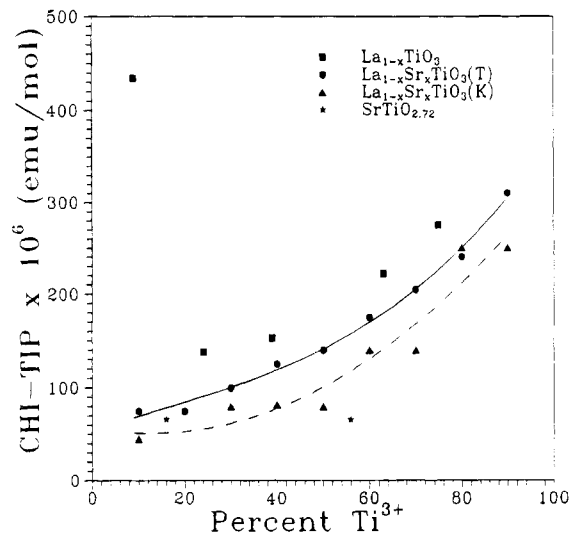


Figure 15. Dependence of χ_{TIP} on Ti^{3+} concentration for $\text{La}_{1-x}\text{TiO}_3$, $\text{La}_{1-x}\text{Sr}_x\text{TiO}_3$ from two sources, (T)⁴ and (K)¹, and $\text{SrTiO}_{2.72}$.

reflecting the occurrence of an insulator-to-metal transition in the former at $\text{La}_{0.75}\text{TiO}_3$ or 24% Ti^{3+} . Into the metallic regime χ_{TIP} values for $\text{La}_{1-x}\text{TiO}_3$ consistently exceed those for $\text{La}_{1-x}\text{Sr}_x\text{TiO}_3$ by about a constant value of $45 \times 10^{-6} \text{ cm}^3 \text{ mol}^{-1}$ at each Ti^{3+} concentration, but the global trend is similar. This suggests a somewhat higher level of correlation in the d electrons for the $\text{La}_{1-x}\text{TiO}_3$ series which is consistent with the analysis of the resistivity results.

Finally, results for the single composition $\text{SrTiO}_{2.7}$ are also plotted. Two entries are listed reflecting an ambiguity which exists for this material. The nominal Ti^{3+} concentration is 56% as fixed by the O^{2-} ion vacancy levels, but the carrier density measured by the Hall method is much lower by nearly a factor of 4 at 16%. Note that the observed χ_{TIP} value is more consistent with the results for $\text{La}_{1-x}\text{Sr}_x\text{TiO}_3$ when the lower level is assumed.

Summary and Conclusions

The solid solution $\text{La}_{1-x}\text{TiO}_3$ is found to exist over the range $0.0 \leq x \leq 0.33$. Three different structure types have been identified, $Pbnm$, $Ibmm$, and $Pban$, the latter describes $\text{La}_{0.67}\text{TiO}_3$ and $\text{La}_{0.70}\text{TiO}_3$ and represents a new perovskite related structure. It is argued that oxidized forms of LaTiO_{3+x} with the perovskite structure are best described as $\text{La}_{1-x}\text{TiO}_3$. The compositions $\text{La}_{0.67}\text{TiO}_3$ and $\text{La}_{0.70}\text{TiO}_3$ are insulating, $\text{La}_{0.75}\text{TiO}_3$ undergoes a metal/insulator transition, and $\text{La}_{0.80}\text{TiO}_3$ and $\text{La}_{0.92}\text{TiO}_3$ are metallic. Evidence from the electrical resistivity and magnetic susceptibility data indicate a greater degree of electron correlation in the metallic members of the series than in the related series $\text{La}_{1-x}\text{Sr}_x\text{TiO}_3$ for the same formal Ti^{3+} concentration.

Acknowledgment. We acknowledge the Natural Science and Engineering Research Council of Canada for funding via a Research Grant and McMaster University for direct support of the McMaster Nuclear Reactor. We thank Professor C. V. Stager for use of the SQUID magnetometer.

Supplementary Material Available: Observed and calculated structure factors for $\text{La}_{0.67}\text{TiO}_3$ and $\text{La}_{0.75}\text{TiO}_3$ (5 pages). Ordering information is given on any current masthead page.